ChemElectroChem

Research Article
doi.org/10.1002/celc.202201122

Chemistry Europe
European Chemical
Societies Publishing

www.chemelectrochem.org

Electrodeposition of Ni–Rh Alloys and their Use as Cathodes for Nitrate Reduction in Alkaline Solutions

Luca Mattarozzi,* Sandro Cattarin, Nicola Comisso, Marco Musiani, Lourdes Vázquez-Gómez, and Enrico Verlato[a]

Compact Ni–Rh alloys are electrodeposited potentiostatically on rotating disk and sheet electrodes; film compositions are adjusted by varying bath composition and deposition potential E_{dep}. SEM images of these alloys show a compact, globular morphology for Rh contents up to 30 at%, and a smoother aspect for films with a medium-to-high content of Rh. XRD spectra show the formation of a single crystalline phase, with diffraction peaks in intermediate positions between those of the constituent elements. Data analysis indicates that crystal lattice parameters vary with composition according to Vegard's law. Linear voltammetries of nitrate reduction in alkali highlight a maximum of activity, in terms of reduction current, for alloys in the range of 10–30 at.% Rh. Prolonged electrolysis at appropriate potential performed with $Ni_{85}Rh_{15}$ alloy shows, in comparison with pure Ni and pure Rh: much increased activity and faster abatement of nitrate; lower production of the undesired nitrite species; higher selectivity towards production of ammonia.

Introduction

Electrochemical reduction of nitrate, a common and ubiquitous pollutant of waters, has been for decades the object of intensive investigation.[1] Whereas the direct conversion to dinitrogen appears impervious,[2] reduction to ammonia, a versatile compound valuable in fertilizer production and other technologies, has been obtained with good yields on several monometallic[3] and bimetallic[4] cathodes and on various spinel oxides modified with either metal[5] or oxygen[6] vacancies and with heteroatoms like Ni[7] and Zn[8] as a substituent in the metal site.

Disregarding cost considerations, Rh has proved to be the most efficient metal element for nitrate electro-reduction.[3c,g] We propose investigations in alkaline solutions considering that: a) both Ni and Rh are stable in this environment, whereas Ni is not stable in acidic solutions; b) the process of nitrate reduction causes release of OH⁻ that may in turn cause pH drift in neutral media;[4e] c) literature investigations reported that Rh-modified electrodes[3i,4d] and Cu-based binary alloys with Rh[4c,j] show excellent performances for nitrate reduction in alkaline solutions. In the latter media, Ni is one of the most investigated cathode materials,[3a,d,4e] together with coinage elements like Cu[4e,f,g] and Ag,[4k] for its good performances, low cost and remarkable stability. To the best of our knowledge, no reports are available in the literature concerning the performances of bimetallic Ni–Rh alloys, and our study will be reported in the following. We deposited a controlled amount of precious Rh in a Ni matrix trying to obtain an electrode material with improved catalytic properties at a still reasonable cost.

The electrodeposition of a bimetallic Ni–Rh alloy is little investigated in the literature;[9] the most recent report is the deposition from a chloride bath, and shows evidence of heterogeneous morphologies and amorphous structures, without any diffraction signal of pure Ni, Rh or other phases related to these elements.[9b] Preparation via metallurgical[10] and chemical[11] routes has been reported to produce a substitutional solid solution in the entire range of compositions, with limited deviations with respect to Vegard's law.

The first aim of this work was to electrodeposit Ni–Rh films with homogeneous morphology and, possibly, crystalline structures. The electrodeposition has been performed from a sulfate bath; the alloy composition was varied by changing bath content and deposition potential and the deposits were characterized in morphology (SEM), composition (EDS) and structure (XRD). Finally, the obtained Ni–Rh layers were used as cathodes for nitrate reduction in alkaline media.

Results and Discussion

Preliminary LSV investigations on Ni–Rh deposition

LSV were recorded on Au-RDE (400 rev min⁻¹, see Figure 1) in three different sulfate solutions with pH 3.0, containing: i) 5 mM $Rh_2(SO_4)_3$ + 0.5 M Na_2SO_4 for Rh deposition; ii) 250 mM $NiSO_4$ + 0.5 M Na_2SO_4 for Ni deposition; and iii) 5 mM $Rh_2(SO_4)_3$ + 250 mM $NiSO_4$ + 0.5 M Na_2SO_4 for Ni–Rh deposition.

The LSV recorded in solution i), continuous red line, shows the start of Rh deposition at potentials somewhat negative to −0.20/−0.25 V, then an extended diffusion plateau of deposi-

ChemElectroChem

Research Article
doi.org/10.1002/celc.202201122

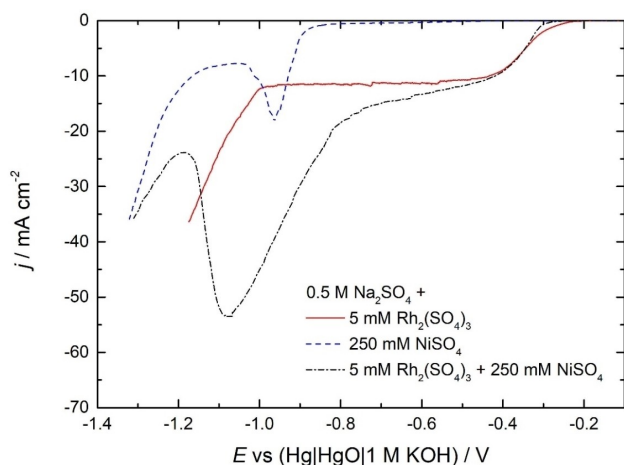**Chemistry
Europe**
European Chemical
Societies Publishing

Figure 1. LSVs (10 mV s^{-1}) recorded at Au RDEs (400 rev min^{-1}) in 0.5 M Na$_2$SO$_4$, pH 3.0 with Rh^{3+} only (continuous red line), Ni^{2+} only (dashed blue line) and, both Rh^{3+} and Ni^{2+} ions (dash-dot black line).

tion until −1.00 V, followed by a marked current increase due to the hydrogen evolution reaction (HER).

In solution ii), dashed blue line, the onset of significant reduction current of Ni deposition occurs at potentials negative to −0.50 V, reaching the peak value of about −18 mA cm^{-2} at −0.95 V, then the current passes through a marked minimum before the onset of vigorous hydrogen evolution at potentials negative to −1.10 V. This type of decrease of Ni deposition current was already observed in our previous work on Ag–Ni alloys, in a similar sulfate solution without a complexing agent.[4k] The decrease in Ni deposition rate may be tentatively attributed either to surface blocking processes caused by hydrogen adsorption (as in self-limited depositions of Pt[12]), or to hydroxides precipitation (due to local cathode alkalinization, as in certain self-terminated depositions of Fe-group metals[13]).

The voltammetric pattern recorded in solution iii) containing both Rh and Ni ions (dash-dot black line) shows features common to the deposition of both single metals. The onset of deposition current occurs in the same potential range (−0.25/−0.30 V) observed for deposition of pure Rh, with only a minor shift to negative potentials attributable to initial inhibition of Rh electrodeposition due to NiSO$_4$ presence. The plateau observed for deposition of pure Rh, red line, becomes a leaning pseudo-plateau in which the cathodic current increases during the negative potential scan, as a result of the progressive activation of Ni–Rh co-deposition. It is known that, when a binary M1–M2 alloy is formed on a cathode, the co-deposition of the less noble metal M1, Ni in this case, is thermodynamically favoured with respect to the deposition of the pure M1 metal. Indeed, according to Kröger,[14] the potential E$_{M1}$ for quasi-static deposition of M1 in the alloy is given by

$$E_{M1} = E^0_{M1} + \frac{RT}{mF} \ln\left(\frac{a_{M1^{m+}}}{a_{M1}}\right) \qquad (1)$$

The activity of M1 in the alloy is always $a_{M1} < 1$. Hence, M1 deposition as an alloy component occurs, according to eq. (1),

at potentials less negative than for pure M1, with a potential gain that is larger for lower M1 molar fractions. After the pseudo-plateau, negative to −0.80 V, the curve shows a large cathodic peak similar to that observed for Ni deposition, then a current drop and a further increase due to activation of hydrogen evolution. The peak shape and size in comparison with the curve of Ni deposition (onset at less negative potential, ca. 3 times higher peak current) are probably the result of the enhanced Ni co-deposition rate mentioned above and of an increased real surface area of the deposits, caused by the Rh deposition that occurs under diffusion control. Ni^{2+} concentration is quite large, so Ni^{2+} transport is not expected to be rate-limiting and the Ni deposition is likely to occur under kinetic control, thus being proportional to the true surface area. The peak potential appears shifted by about 0.1 V in a negative direction (as compared to the Ni deposition peak), a shift accounted for by the uncompensated ohmic drop, due to an electrolyte resistance of 1.75 Ω cm^2.

Further voltammetric investigations were conducted on the behaviour of Rh^{3+} in sodium sulfate solution, with pH regulated to 3.2 to avoid any interferences by H$^+$ reduction.[15] In detail, LSVs on Au-RDE were recorded at several rotation speeds (100–400–900 rev min^{-1}, Figure 2a). Figure 2b presents a plot show-

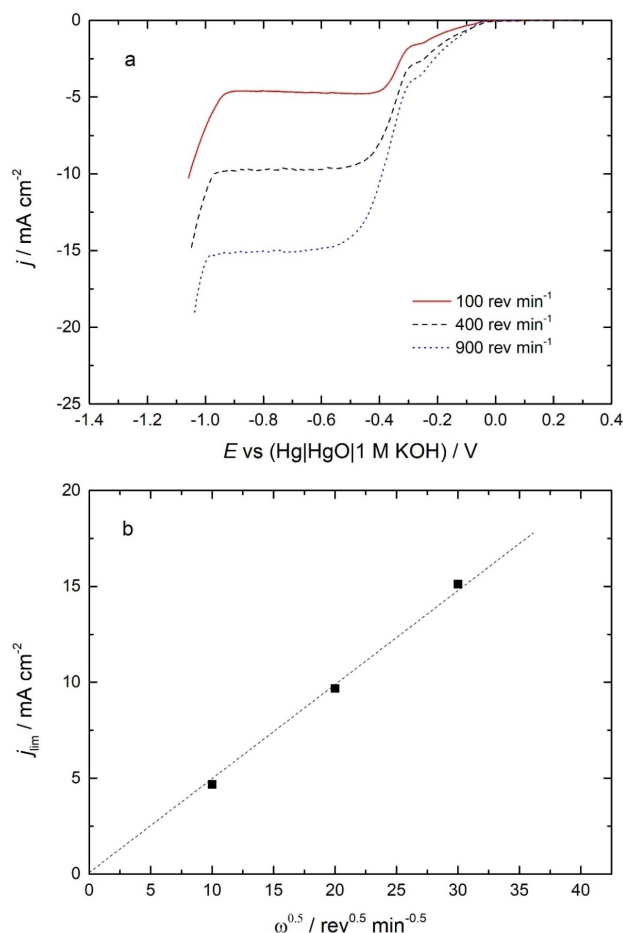**Figure 2.** a) LSVs (10 mV s^{-1}) recorded at Au RDEs (400 rev min^{-1}) in 5 mM Rh$_2$(SO$_4$)$_3$ + 0.5 M Na$_2$SO$_4$, pH 3.2 (Bath II, Table 1), at different rotational speeds. b) Levich plot of plateau current densities.

ChemElectroChem

Research Article
doi.org/10.1002/celc.202201122

Chemistry Europe
European Chemical
Societies Publishing

ing that the plateau currents (sampled at −0.70 V, in the middle of the plateau) vary linearly with the square root of the rotation speeds, in agreement with the Levich behaviour valid for diffusion limited currents:

$$j_{lim} = 0.62 \ n \ F \ A \ D^{2/3} \ \nu^{-1/6} \ \omega^{1/2} \ C_0 \tag{2}$$

where in this case: $n = 3$ is the electronicity of the process, F is the Faraday constant (96485 C mol^{-1}), A is the disk electrode area in cm^2, D is the diffusion coefficient of the species (Rh^{3+} ions) in cm^2 s^{-1}, ν is the kinematic viscosity of the solution (0.01 cm^2 s^{-1},[16]), ω is the rotation speed (in rad s^{-1}) and C_0 is the concentration of the considered species in the bulk (10× 10^{-6} mol cm^{-3}). Using the plot of j_{lim} vs $\omega^{1/2}$ reported in Figure 2b, and the relation in eq. (2), the diffusion coefficient D for Rh^{3+} ion was calculated to be c.ca 7.6×10^{-6} cm^2 s^{-1}, in substantial agreement with data reported by Pletcher for sulfate solution (6.9×10^{-6} cm^2 s^{-1},[15]) and by Yu and Sohn for chloride solution (6.3×10^{-6} cm^2 s^{-1},[17]).

Ni−Rh electrodeposition – SEM and EDS characterizations

Compact films of Ni, Rh and Ni−Rh alloys were electrodeposited potentiostatically on Au-RDEs (400 rev min^{-1}) using the solutions listed in Table 1 (three top lines); the deposition potentials E_{dep} and the compositions determined by EDS are reported in Table 2.

The deposition potentials were fine-tuned to obtain regularly distributed Ni−Rh compositions (Table 2), e.g. from Ni$_{90}$Rh$_{10}$ to Ni$_{50}$Rh$_{50}$. Ni was deposited from a Watt bath which warrants production of a bright compact film. Rh was deposited from a sulfate bath (similar to that used for alloys' depositions). SEM pictures of pure Ni (Figure 3A) and pure Rh (Figure 3F) films show compact morphologies. Considering now Ni−Rh alloys and in particular the Ni-rich ones (Ni$_{90}$Rh$_{10}$), the deposit appears dull to the naked-eye, and in electronic image (Figure 3B) shows globular but compact surface morphology. Deposition at less negative potentials E_{dep} causes an increase of Rh content in the films (Table 2), resulting in a tinier globular structure and a flatter overall morphology in SEM images (Figure 3C, 3D). Deposits with a Ni content in the order of 50 at. % (Figure 3E)

Table 1. Composition of baths used for electrodepositions.

Bath	Composition
Watt	1.126 M NiSO$_4$ + 0.185 M NiCl$_2$ + 0.485 M H$_3$BO$_3$
I	5·10^{-3} M Rh$_2$(SO$_4$)$_3$ + 0.25 M NiSO$_4$ + 0.5 M Na$_2$SO$_4$
II	5·10^{-3} M Rh$_2$(SO$_4$)$_3$ + 0.5 M Na$_2$SO$_4$
III	4·10^{-3} M Rh$_2$(SO$_4$)$_3$ + 0.25 M NiSO$_4$ + 0.5 M Na$_2$SO$_4$

Table 2. Electrodeposition of Ni, Ni−Rh alloys and Rh on Au-RDEs. Bath compositions are reported in Table 1. Other details may be found in the experimental section.

Sample	E_{dep}/[V]	Bath	EDS comp. at.% (Au-RDE)
A	galvanostatic at −8 mA cm^{-2}	Watt	Ni
B	−0.950	I	Ni$_{90}$Rh$_{10}$
C	−0.810	I	Ni$_{81}$Rh$_{19}$
D	−0.710	I	Ni$_{69}$Rh$_{31}$
E	−0.570	I	Ni$_{50}$Rh$_{50}$
F	−0.300	II	Rh

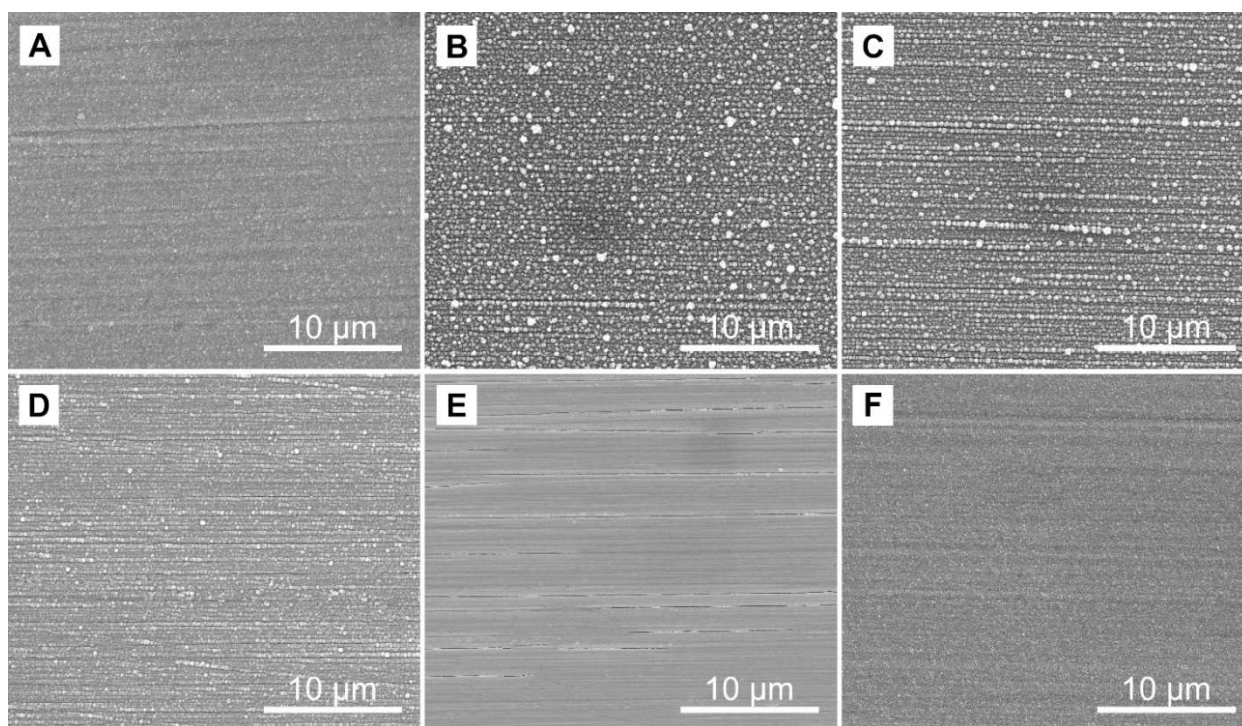**Figure 3.** SEM images of sample A (Ni), B (Ni$_{90}$Rh$_{10}$), C (Ni$_{81}$Rh$_{19}$), D (Ni$_{69}$Rh$_{31}$), E (Ni$_{50}$Rh$_{50}$) and F (Rh). Details regarding experimental conditions are reported in Table 2.

ChemElectroChem

Research Article
doi.org/10.1002/celc.202201122

Chemistry
Europe
European Chemical
Societies Publishing

or below are relatively bright to naked eye observation, showing a light gray metallic surface. All the EDS spectra reveal only a little presence of oxygen, excluding a significant formation of oxides during electrodeposition or afterwards.

For the sake of comparison with the films obtained on rotating disk electrodes, a series of Ni–Rh alloy samples was electrodeposited on Au-sheets for XRD structural analyses. Preliminary electrodeposition tests showed that, operating at the same E_{dep} values, alloy films systematically richer in Rh were obtained on Au-sheets than on Au-RDEs. A modified bath III, with a lower Rh^{3+} concentration (Table 1), was necessary to permit deposition of Ni-rich alloys on Au-sheets; all the depositions potentials were redefined to obtain a series of Ni–Rh alloys regularly distributed in composition (Table 3).

The morphologies of films on Au-sheet substrate are comparable with those observed for deposition on RDE. Gravimetric evaluations on Ni–Rh films deposited on Au-sheet show, within the limits of experimental accuracy, that the faradaic efficiency of deposition is between 60 and 80% for all the considered samples.

XRD structural characterization of Ni–Rh alloys

The compact Ni–Rh films were investigated by X-Ray diffraction. The recorded spectra are reported in Figure 4a; at the bottom are reported the diffraction peak positions of pure Rh,[18] pure Ni[19] and Au substrate[20] as from their ICDD cards. At variance with previous findings regarding Ni–Rh films from chloride bath, reported to be amorphous,[9b] all the considered spectra show diffraction peaks located at 2θ values that are intermediate between those of pure Ni and pure Rh and vary in position, shifting regularly towards lower angles on increasing the content of Rh from sample L to O. On this basis, from the three most intense diffraction peaks, (111), (200) and (220), the lattice parameter a for face centred cubic structure (fcc) (i.e. the crystalline structure of Ni and Rh) was calculated for each deposited Ni–Rh films. As shown by Figure 4b, the a value varies linearly with film composition, in accordance with the Vegard's law. This evidence confirms the formation of single homogeneous bimetallic phase (solid solution) for each electro-deposited sample of Ni–Rh films.
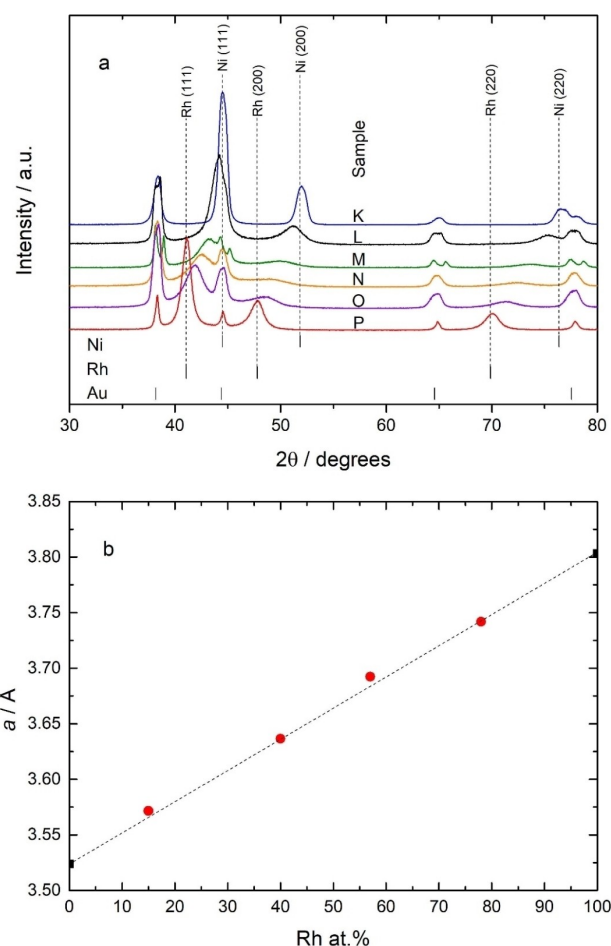

Figure 4. a) XRD spectra of pure Ni, Ni–Rh alloys and pure Rh deposited on Au-sheet substrates (see Table 3 for details). b) Crystal lattice parameter a of Ni–Rh alloys (red dots), calculated from experimental diffraction patterns; a values for pure Rh[12] and pure Ni[13] (black square dots) calculated from ICDD cards data.

LSV of nitrate and nitrite reduction in 1 M NaOH

A preliminary linear sweep voltammetric investigation (Figure 5) was performed to characterize the behaviour of pure Ni and pure Rh towards nitrogen oxyanions' reduction in 1 M NaOH. Both Ni and Rh are quite active towards reduction of 20 mM nitrate, but show different features. By sweeping the potential of a Ni electrode (blue line) from open circuit in a negative direction, we observe the onset of nitrate reduction at −0.95 V, then a rapid increase of current until −1.25 V, a pseudo-plateau ($j \cong -30$ mA cm^{-2}) and a further current increase due to onset of hydrogen evolution. On the other hand, the good activity of Rh (red line) for nitrate reduction (reported in acidic media[3g]) is confirmed in alkaline solution by the early onset at the potential of ca. −0.70 V. The voltammetric curve continues with a rather low current peak at −0.86 V, not much higher than that observed in the base electrolyte at more negative potential, due to H adsorption (red dotted line), a minimum and a final new rise due to overlapping of the HER with the nitrate reduction process.

Table 3. Electrodeposition of Ni, Ni–Rh alloys and Rh on sheet electrodes (solutions magnetically stirred) used for XRD investigations and electrolysis experiments. Bath compositions are reported in Table 1; other details may be found in the experimental section.

Sample	E_{dep}/[V]	Bath	EDS comp. at.% (Au-sheet)
K	galvanostatic at −8 mA cm^{-2}	Watt	Ni
L	−0.950	III	Ni$_{85}$Rh$_{15}$
M	−0.690	I	Ni$_{60}$Rh$_{40}$
N	−0.570	I	Ni$_{43}$Rh$_{57}$
O	−0.440	I	Ni$_{22}$Rh$_{78}$
P	−0.300	II	Rh

ChemElectroChem

Research Article
doi.org/10.1002/celc.202201122
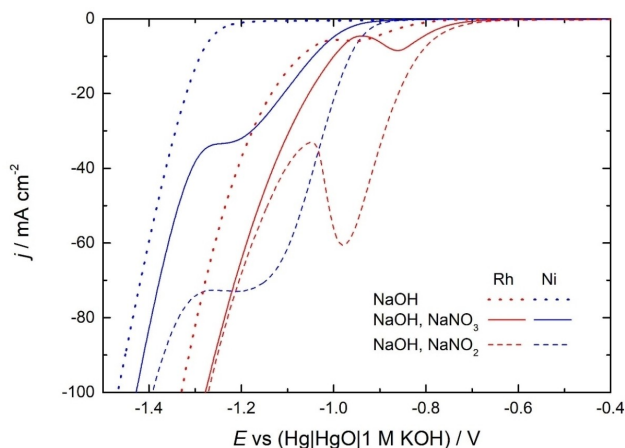
Chemistry Europe
European Chemical
Societies Publishing

Figure 5. Forward scan LSVs ($v_{scan} = 20$ mV s^{-1}, $\omega = 900$ rev min^{-1}) on RDE covered by pure Rh (red) and pure Ni (blue) in 1 M NaOH (dotted lines); in 1 M NaOH + 20 mM NaNO$_3$ (continuous lines) and in 1 M NaOH + 20 mM NaNO$_2$ (dashed lines).

The LSV curve of nitrite reduction recorded on Ni (Figure 5, blue dashed line) shows a current onset at −0.90 V, slightly anticipated in comparison to nitrate, followed by a current rise up to a diffusion plateau between −1.2 and −1.3 V, with a limiting current of ca. −75 mA cm^{-2}. In a previous paper,[4e] we reported voltammetric curves of nitrate/nitrite reduction on Ni recorded at different scan rates, which provided evidence of (i) faster kinetics for nitrite than for nitrate reduction, (ii) low average electronicity for nitrate reduction and (iii) for both anions, possible surface blocking by reaction intermediates.

The reduction of nitrite on Rh (Figure 5, red dashed line) starts at c.ca −0.70 V and shows a prominent current peak, ca. −60 mA cm^{-2} at −0.98 V, in the same region where the hydrogen adsorption takes place (see electrolyte curve, red dotted line). It is known from literature that on Rh, the nitrate reduction process is partially hindered by hydrogen adsorption[3i] and that, at more negative potentials, this process becomes a H-source[4m] for hydrogenation of oxygenated N-species reduced mainly to ammonia.[4j]

The study continued on the process of nitrate reduction in 1 M NaOH at Ni–Rh alloys, comparing the relevant voltammetries (Figure 6a) with those recorded at electrodes of the pure elements Ni (Figure 6a, blue line) and Rh (Figure 6a, red line). The voltammetric pattern recorded at Ni$_{90}$Rh$_{10}$ (Figure 6a, green line) shows the onset of nitrate reduction at a potential intermediate between those of the metals, about 100 mV positive to that on pure Ni. On sweeping the potential further in a negative direction, the rise in current appears to result from both nitrate reduction and hydrogen evolution, which respective contributions are discussed below based on the analysis of the reduction reaction products. Voltammetric curves recorded at alloys with higher Rh content up to ca. 20 at.% show a further shift to less negative values; however, at still higher Rh content the trend inverts and on increasing the Rh percentage the activity decreases (Figure 6a, purple line). If we select −50 mA cm^{-2} (Figure 6a, dotted horizontal line) as a convenient practical current density for nitrate abatement, and we plot the
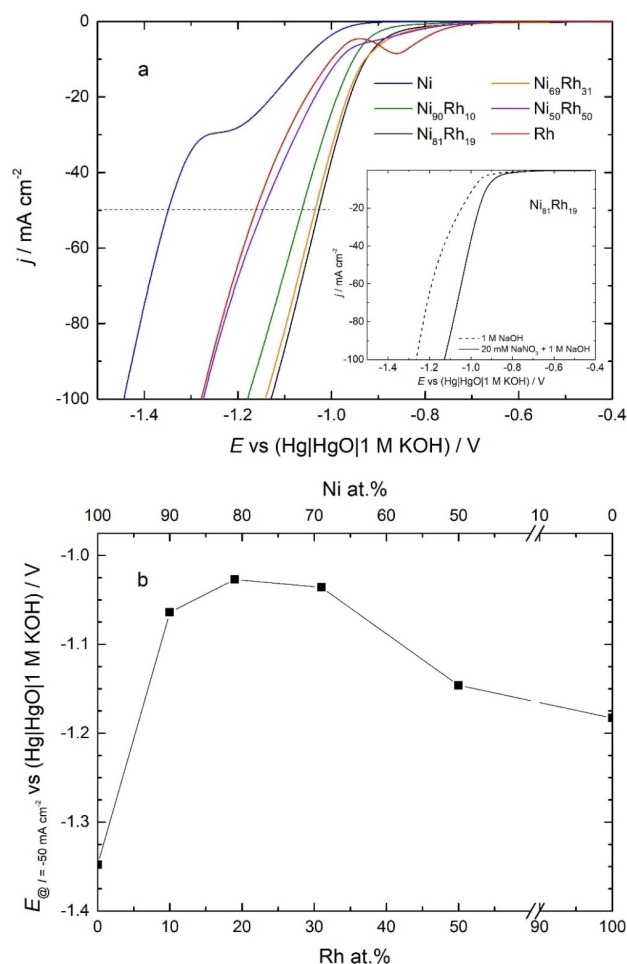

Figure 6. a) Forward scan LSVs ($v_{scan} = 20$ mV s^{-1}, $\omega = 900$ rev min^{-1}) on RDE of indicated compositions (Table 2) recorded in 1 M NaOH + 20 mM NaNO$_3$; the dotted line is at $j = -50$ mA cm^{-2}. The inset compares LSVs recorded on Ni$_{81}$Rh$_{19}$ electrodes in the alkaline electrolyte, with and without nitrate; b) Dependence of E (from LSVs) at $j = -50$ mA cm^{-2} on RDE composition of Ni–Rh films (assessed by EDS).

corresponding potentials for each material as a function of Ni–Rh alloy composition, a broad maximum, i.e. an overpotential minimum, is observed for alloys with Rh contents between 10 and 30 at.% (Figure 6b). The inset in Figure 6a shows the presence of a potential window between ca −1.05 V and −1.2 V in which NO$_3^-$ reduction on Ni$_{81}$Rh$_{19}$ is predominant over hydrogen evolution. The phenomenology shown by Figure 6 testifies a synergy between the two alloy elements similar to that already observed by our group with Cu–Rh electrodeposited thin film cathodes[4c] and by Mirzaei et al. with Cu–Rh nanoparticles/C composite electrodes.[4j] Synergetic effects have been previously observed also with Sn-modified Rh nanoparticles:[4h] partial Sn coverage of the Rh surface enhanced the electrode activity in the nitrate reduction, however the reduction current decreased upon complete Sn coverage.

Since a limited fraction of Rh, say 10–15 at%, may cause a marked increase in the activity of the Ni–Rh alloy in comparison with pure Ni for a limited extra cost of the precious element, we decided to conduct prolonged electrolyses on electrodes

consisting of pure Ni, pure Rh, and $Ni_{85}Rh_{15}$ alloy, easily obtained on Au sheets (sample L, Table 3). This composition is not present in the series of RDEs samples collected in Table 2, and tested in LSV experiments of Figure 6. However, the reported LSVs of $Ni_{90}Rh_{10}$ and $Ni_{81}Rh_{19}$ are sufficiently similar to provide a reliable description of the activity of the alloy $Ni_{85}Rh_{15}$, with a composition intermediate between those studied by LSV.

Prolonged electrolyses of nitrate in alkaline media. Assessment of reduction products

Electrolyses lasting 6 hours were conducted in a magnetically stirred solution of 20 mM $NaNO_3$ in 1 M NaOH. Sheet electrodes of Ni, Rh and $Ni_{85}Rh_{15}$ alloy were polarized at $E = -1.20$ V, a convenient compromise potential warranting that: little hydrogen evolution occurs on Ni (Figure 5), that may be therefore considered a useful term of comparison; fairly large currents flow on Rh and Rh-containing alloys, presumably providing good nitrate reduction rates. The chronoamperometric curves of electrolyses are reported in Figure 7 and present a common
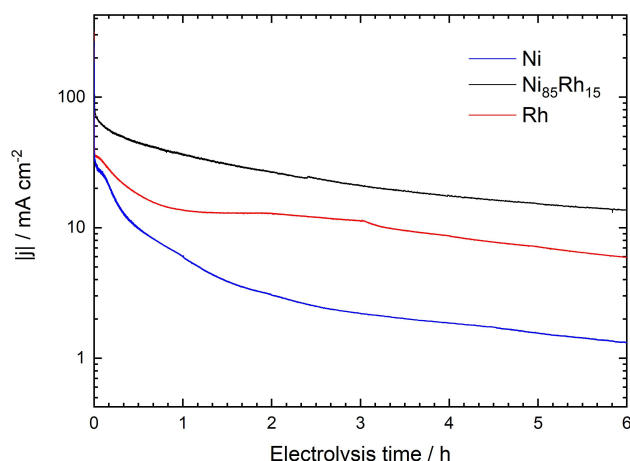

Figure 7. Chronoamperometric curves recorded at selected sheet electrodes during constant potential electrolyses ($E = -1.20$ V) in 1 M NaOH + 20 mM $NaNO_3$ (V = 100 mL), gently agitated by magnetic stirrer.

pattern: a current spike at early times upon potential application; a rapid initial decay (in absolute values); a subsequent slower but steady current decrease. A part of the current decrease is due to the progressively lower concentrations of unreacted nitrate ions at increasing electrolysis durations. The relative values of the reduction currents reflect the LSVs of Figure 6a.

Ni electrode (Figure 7, blue line) shows chronoamperometric curves with an absolute cathodic current exceeding 20 mA cm^{-2} in the first minutes of electrolysis, then declining rapidly in the first hour and steadily thereafter: at the end of the 6 hours experiment, a final value of ca. 1.5 mA cm^{-2} is attained.

The chronoamperometry at pure Rh (Figure 7, red line) shows a starting current above 30 mA cm^{-2} (in absolute value), a fast initial decay followed by a quasi-plateau between 1 and 3 hours; then a slow steady decrease to the end value of about 6 mA cm^{-2}.

The current curve recorded at the $Ni_{85}Rh_{15}$ alloy electrode (Figure 7, black line), shows the largest (absolute) initial current of ca. 80 mA cm^{-2}, then currents steadily exceeding those recorded at both parent metals during the entire polarization experiment. From 2 h onwards, the current is about ten times higher than that recorded at the pure Ni electrode and is still ca. 15 mA cm^{-2} after 6 h.

Assessment of nitrate reduction products was performed by ion chromatography. All the collected chromatograms show i) for cations' analyses, only peaks pertinent to sodium and ammonium (i.e. protonated ammonia) and ii) for anions' analyses, only peaks due to nitrate and nitrite.

Table 4 reports, for the 3 tested materials, the amount of charge passed at the moment of the test t, the concentrations of the main chemicals and the selectivity, namely the ratio between the concentration of the main identified products and that of the converted nitrate.

Some data are reported for a more direct illustration in Figure 8. Figure 8a shows the residual nitrate concentration estimated at time t for the three electrodes; Figure 8b reports the current efficiency for the production of any given species, i.e. the ratio between the charge used to produce it and the total electrolysis charge. The contribution of "Other" to the sum

Table 4. Ion chromatographic data relative to prolonged electrolyses at E = −1.20 V in 1 M NaOH + 20 mM $NaNO_3$ (100 mL) of the three tested materials: Ni, Rh, and $Ni_{85}Rh_{15}$ alloy. Cathodic charges are reported in absolute value.

Electrode material	t/[h]	Charge/C	$[NO_3^-]_t / \cdot 10^{-3}$ M	$[NO_2^-]_t / \cdot 10^{-3}$ M	$[NH_3]_t / \cdot 10^{-3}$ M	* Selectivity % to NO_2^-	* Selectivity % to NH_3
Ni	1	48.2	18.80	0.75	0.40	62.5	33.3
	2	62.9	18.40	0.95	0.50	59.4	31.3
	4	82.6	18.00	1.05	0.60	52.5	30.0
	6	91.2	17.80	1.15	0.65	52.3	29.5
Rh	1	76.4	19.45	0.25	0.20	45.5	36.4
	2	123.4	19.10	0.40	0.35	44.4	38.9
	4	201.6	18.20	0.70	0.70	38.9	38.9
	6	253.0	17.75	0.85	0.85	37.8	37.8
$Ni_{85}Rh_{15}$	1	174.8	17.95	0.20	1.70	9.8	82.9
	2	286.6	16.60	0.35	2.75	10.3	80.9
	4	440.6	15.05	0.55	3.95	11.1	79.8
	6	551.6	13.85	0.65	4.85	10.6	78.9

* Selectivity: ratio % between moles of nitrite/ammonia produced and moles of converted nitrate (see text)

ChemElectroChem

Research Article
doi.org/10.1002/celc.202201122

Chemistry Europe
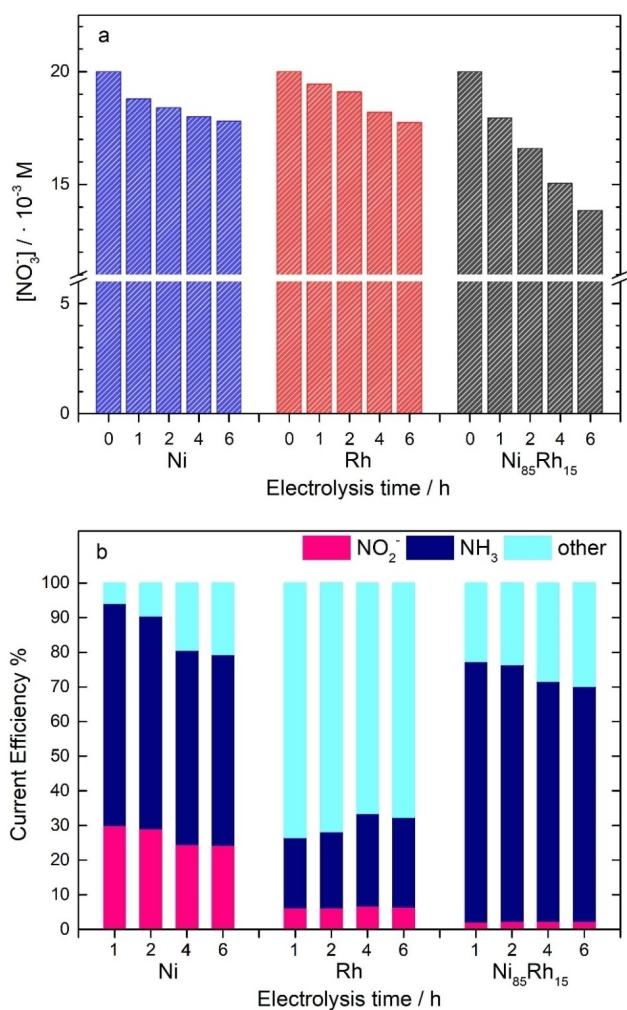European Chemical
Societies Publishing

Figure 8. a) Residual nitrate concentrations detected at sampling times t after electrolysis at $E = -1.2$ V; b) current efficiency: charge necessary to generate the amount of product as a % of total charge used. "Other" represents undetected species, presumably mostly H_2.

of 100% represents the charge not justified by detected nitrite or ammonia, and may be attributed to the parasitic process of hydrogen evolution and, possibly, to the loss of some volatile N products due to a non-perfectly tight cell.

In agreement with the low current observed in the chronoamperometry of Figure 7, a low charge is passed at the Ni electrode during the 6-hours electrolysis, with a limited abatement of nitrate (Figure 8a) and a significant contribution of the 2-electrons reduction to nitrite instead of the 8-electrons reduction to ammonia. The good outcome of using the Ni electrode is the fairly low charge wasted in parasitic processes. However, this advantage at early times (only 5.9% of charge dispersed during the first h) decreases steadily on prolonging the electrolysis (20.7% of dispersion after 6 h), presumably due to a comparatively faster decay of nitrate reduction than of hydrogen evolution. The low activity, together with the large yield of nitrite (Figure 8b), a worse pollutant than the original nitrate, make this cathode unsuitable for the reduction of nitrate in alkali.

The electrolysis at Rh cathode causes larger charge transfer in comparison with Ni, but at least two thirds of it results in hydrogen evolution (Figure 8b), due to intrinsic good catalytic performance in HER. The reduction process turns out to be of little practical value, as it causes: a small decrease in the concentration of nitrate; a significant production of undesired nitrite; a current efficiency only in the range 20–30% for production of ammonia.

The electrolysis at the $Ni_{85}Rh_{15}$ cathode shows transfer of the largest integrated charge in the series. The analyses performed on the solution show also the best results: the highest abatement of nitrate; a fairly low production of nitrite; a large production of ammonia, that represents at all times about 80% of the converted nitrate and accounts for most of the applied reduction charge. Hence, at the selected electrolysis potential of $E = -1.2$ V, the prevalent reaction pathway leads to the fully hydrogenated product (NH_3) on both Ni and Rh. The same apparently happens on the alloy, to the exclusion of significant amounts of other products (e.g. NH_2OH or N_2H_4). The parasitic charge, presumably used for hydrogen evolution, is relatively low and comparable with that observed using Ni cathodes. Combining the highest nitrate conversion (ca. three times higher than pure metals for a 6 hours treatment) with a moderate current decline in time (comparable to that observed on Rh and significantly lower than observed on Ni) the Ni–Rh alloy is the cathode material least prone to poisoning.

We did not perform long term stability tests under conditions of practical application. However, we stress that: both Ni and Rh are known to be stable in the considered medium; no evidence of morphological modification of electrode surface was obtained by SEM investigations after electrolyses; the alloy offers better current stability than Ni (Figure 7) and comparable with that of Rh; a current decay of the type observed in Figure 7 is frequently observed in the literature and attributed to surface blocking.[3k,4j] More extensive tests (like those reported e.g. in[5–8]) are beyond the scope of the present investigation and may be the object of future extended work.

A comparison of the reaction products of nitrate reduction obtained in this work with $Ni_{85}Rh_{15}$ cathodes and in a previous work with Rh-modified Ni foam electrodes[4d] shows a marked prevalence of ammonia in both cases, although Ni and Rh were mixed at the atomic scale in the former case (solid solution) but not in the latter (Rh nanoparticles deposited on Ni surface). We may conclude that Ni, able to promote nitrate reduction mainly to nitrite and, in a minor amount, to ammonia, and Rh, able to catalyse H transfer,[4m] seemed to operate in a synergetic way in the $Ni_{85}Rh_{15}$ alloy, analogously to what has been suggested by Mirzaei et al.[4j] for composite electrodes based on C-supported Cu–Rh nanoparticles. Since the close proximity between Ni and Rh atoms appears essential to generate the observed synergetic effects, one may speculate that, in the case of Rh-modified Ni foam electrodes, the most active sites were probably those located along the periphery of Rh nanoparticles in contact with both the Ni foam support and the electrolyte.

Conclusions

We have presented the electrodeposition of Rh metal and Ni–Rh alloys from a sulfate bath in a wide range of compositions: pure Rh, Rh-rich alloys, equimolar Ni–Rh and Ni-rich alloys, adjusting bath composition and deposition potential E_{dep}. The morphologies of the alloys are globular at low Rh content, up to about 30 at%, and flatten on using more positive electrodeposition potentials E_{dep} that result in an increased content of Rh atoms. XRD analyses show patterns consistent with the formation of a crystalline single phase of substitutional solid solution over the entire range investigated; the lattice parameters vary with composition according to Vegard's law.

The alloy $Ni_{85}Rh_{15}$, selected considering the low content of expensive Rh and the good catalytic activity in RDEs experiments, shows during prolonged electrolyses of nitrate solutions distinct advantages in comparison with pure Ni and Rh elements: i) higher currents, possibly promoted by an increased surface roughness, and a much faster nitrate abatement; ii) the best selectivity towards a single product, i.e. ammonia and iii) a low charge fraction wasted in parasitic processes, presumably H_2 evolution, similar to that of Ni metal and much below that of Rh metal. Increased performance of the alloy may be attributed to the intimate mixing of the two atom types, and specifically to the ability of Rh to ease nitrate reduction, possibly via the hydrogenation of intermediates.

From a practical perspective, the Ni–Rh alloy with a Rh content of 10–15 at% appears a promising material for cathodic reduction of nitrate in alkaline solutions due to its valuable catalytic performances, good chemical stability and reasonable cost.

Experimental Section

Deposition baths and electrodeposition procedures

All metal depositions were performed in solutions prepared from deionized water (by Elga-Veolia Purelab Pulse System, $\rho > 18$ MΩ cm) and high purity metal salts. Ni–Rh alloys' deposition bath contained: $Rh_2(SO_4)_3 \cdot 4H_2O$ (Alfa Aesar Premion®), $NiSO_4 \cdot 6H_2O$ and Na_2SO_4 as supporting electrolyte (Merck-Sigma-Aldrich), pH adjusted to about 3.0. Ni films were obtained by galvanostatic electrodeposition at -8 mA cm^{-2} from Ni Watt's bath (1.126 M $NiSO_4 + 0.185$ M $NiCl_2 + 0.485$ M H_3BO_3). Electrodepositions of Rh and Ni–Rh films were performed under potentiostatic control in a single-compartment cell, compatible with a working volume of 25 ml. The cell featured a 3 electrode assembly, with a Pt flag (3 cm^2) counter-electrode and a saturated calomel reference electrode (SCE, inserted in Luggin capillary, $E_{SCE} = +0.241$ V$_{NHE}$). All the potentials in text and figures are referred to Hg|HgO|1 M KOH ($E_{HgO} = +0.140$ V$_{NHE}$) electrode, for the sake of homogeneity with nitrate reduction experiments. The solutions were kept at 25 °C and deaerated for at least 20 minutes, prior to use. Rh films were deposited at $E = -0.3$ V from a bath of $Rh_2(SO_4)_3 \cdot 4H_2O$ and Na_2SO_4 as supporting electrolyte, pH adjusted to 3.0 as above. The composition of all baths used for electrodepositions is reported in Table 1. The potentials used for the deposition of alloys are reported in Table 2–Table 3.

Potentiostatic/potentiodynamic control was applied with an Autolab PGSTAT 302 N. Preliminary investigations were performed by Linear Sweep Voltammetry (LSV) with RDEs.

Depositions on RDEs were performed at 400 rev min^{-1}, for a charge of 2 C cm^{-2}, on: a) Au-RDEs for preliminary tests of electrodeposition and EDS investigations, to avoid any interference from the substrate; b) Ni-RDEs, to collect SEM images and LSV of nitrate reduction. Au- and Ni-RDEs were both home-made, inserting Au-rod (Goodfellow 99,95%, area 0.07 cm^2) and Ni-rod (Goodfellow 99%, area 0.317 cm^2) in PTFE sheaths and connecting them to an EDI101 rotating unit (Radiometer Copenhagen) with a stainless-steel adapter.

Pure Ni, Ni–Rh and pure Rh films on sheet electrodes were obtained by transferring a deposition charge of 2 C cm^{-2} in a solution gently agitated by magnetic stirring to ensure diffusion conditions similar to those obtained at RDEs. For XRD analyses, alloy films were deposited on Au-sheet substrates; for prolonged nitrate electrolyses, Ni-sheet substrates were used. Prior to deposition, RDEs substrates were polished with emery paper 4000 grit, rinsed with water and polished again with 1 μm alumina. Finally, the rotating disks were rinsed again with water in a water ultrasound bath (15 min) and dried. Sheet electrodes were polished with emery paper 4000 grit, rinsed with water in a water ultrasound bath (15 min) and dried.

Instrumentation for electrode characterization

SEM images were obtained with a FEI Quanta 200 FEG ESEM instrument, equipped with a field emission gun, operating at an accelerating voltage of 25 kV. EDS analyses were performed using an EDAX Genesis energy dispersive X-ray spectrometer.

For XRD analyses, a Malvern Panalytical Empyrean diffractometer with a grazing incidence geometry (fixed incidence angle of 1.0°, 0.025°/step and 500 s/step) was employed to characterize the structure of the synthetized films. Spectra in Bragg-Brentano geometry (0.025°/step and 100 s/step) were also collected; both configurations used a Cu Kα source (40 kV and 40 mA). The peak positions were estimated with the instrumental fitting software Highscore Plus using the standard patterns reported in the 2002 ICDD database.

Nitrate reduction: LSV and prolonged electrolyses

A Hg|HgO|1 M KOH ($E_{HgO} = +0.140$ V$_{NHE}$) was used as reference electrode during electrochemical tests in alkaline environment. All the currents were normalized to the geometric area of the working electrodes. Nitrate and nitrite reduction tests were performed by LSV on RDEs covered by Ni and Rh in a single compartment cell containing respectively 1 M NaOH + 20 mM $NaNO_3$ or 1 M NaOH + 20 mM $NaNO_2$ deaerated solutions; to complete the framework, also LSVs in supporting electrolyte were reported. Ni–Rh alloys of selected compositions were deposited on RDEs and tested for nitrate reduction in 1 M NaOH + 20 mM $NaNO_3$, comparing their behaviour with that of Ni and Rh. Prolonged electrolyses (6 h) of nitrate reduction were performed in a two-compartment cell, containing 100 ml of deaerated 1 M NaOH + 20 mM $NaNO_3$ solution in the magnetically stirred working compartment, with sheets electrodes (working area = 1 cm^2) covered by Ni, Rh and $Ni_{85}Rh_{15}$ compact films. The products were assessed by withdrawing 100 μl samples from the working compartment solution with a precision pipette: for the determination of cations the samples were diluted with water, with an addition of an excess of acid to ensure quantitative formation of the protonated species (e.g. NH_4^+); for the determination of anions NO_3^- and NO_2^-, the electrolyzed

ChemElectroChem

Research Article
doi.org/10.1002/celc.202201122

Chemistry
Europe
European Chemical
Societies Publishing

samples were properly diluted with water. Analyses were performed with a Metrohm model 850 Professional IC Ion Chromatograph according to IC Metrohm Application Notes available online. Main details: for analysis of cations a Metrosep C6-250 2.0 IC column, an eluent solution of 1.7 mM nitric acid with 1.7 mM dipicolinic acid in water and conductivity detector; for analysis of anions, a Metrosep A SUPP 4–250 4.0 IC column, an eluent solution of 1.8 mM $Na_2CO_3 + 1.7$ mM $NaHCO_3$ in water, with chemical suppression and conductivity detector. Linear calibration curves were obtained by injecting diluted solutions containing pre-set concentration of ammonium, nitrate, nitrite and sodium. No direct evaluation was made of N_2 or other gaseous products.

Conflict of Interest

The authors declare no conflict of interest.

Data Availability Statement

The data that support the findings of this study are available from the corresponding author upon reasonable request.

[1] a) V. Rosca, M. Duca, M. T. DeGroot, M. T. M. Koper, *Chem. Rev.* **2009**, *109*, 2209–2244; b) C. Milhano, D. Pletcher, The electrochemistry and electrochemical technology of nitrate, in: R. E. White (Ed.), Modern Aspects of Electrochemistry, vol. 45, Springer, Dordrecht, **2009**.

[2] M. Duca, M. C. Figueiredo, V. Climent, P. Rodriguez, J. M. Feliu, M. T. M. Koper, *J. Am. Chem. Soc.* **2011**, *133*, 10928–10939.

[3] a) H.-L. Li, D. H. Robertson, J. Q. Chambers, D. T. Hobbs, *J. Electrochem. Soc.* **1988**, *135*, 1154–1158; b) H.-L. Li, J. Q. Chambers, D. T. Hobbs, *J. Appl. Electrochem.* **1988**, *18*, 454–458; c) M. Wasberg, G. Horányi, *Electrochim. Acta* **1995**, *40*, 615–623; d) K. Jha, J. W. Weidner, *J. Appl. Electrochem.* **1999**, *29*, 1305–1315; e) D. De, J. D. Englehardt, E. E. Kalu, *J. Electrochem. Soc.* **2000**, *147*, 4573–4579; f) K. Bouzek, M. Paidar, A. Sadílková, H. Bergmann, *J. Appl. Electrochem.* **2001**, *31*, 1185–1193; g) G. E. Dima, A. C. A. de Vooys, M. T. M. Koper, *J. Electroanal. Chem.* **2003**, *554–555*, 15–23; h) G. E. Dima, G. L. Beltramo, M. T. M. Koper, *Electrochim. Acta* **2005**, *50*, 4318–4326; i) O. Brylev, M. Sarrazin, L. Roué, D. Bélanger, *Electrochim. Acta* **2007**, *52*, 6237–6247; j) D. Reyter, D. Bélanger, L. Roué, *Electrochim. Acta* **2008**, *53*, 5977–5984; k) M. Duca, B. Van Der Klugt, M. A. Hasnat, M. Machida, M. T. M. Koper, *J. Catal.* **2010**, *275*, 61–69.

[4] a) M. C. P. M. Da Cunha, J. P. I. De Souza, F. C. Nart, *Langmuir* **2000**, *16*, 771–777; b) B. K. Simpson, D. C. Johnson, *Electroanalysis* **2004**, *16*, 532–538; c) N. Comisso, S. Cattarin, S. Fiameni, R. Gerbasi, L. Mattarozzi, M. Musiani, L. Vázquez-Gómez, E. Verlato, *Electrochem. Commun.* **2012**, *25*, 91–93; d) E. Verlato, S. Cattarin, N. Comisso, L. Mattarozzi, M. Musiani, L. Vázquez-Gómez, *Electrocatalysis* **2013**, *4*, 203–211; e) L. Mattarozzi, S. Cattarin, N. Comisso, P. Guerriero, M. Musiani, L. Vázquez-Gómez, E. Verlato, *Electrochim. Acta* **2013**, *89*, 488–496; f) L. Mattarozzi, S. Cattarin, N. Comisso, R. Gerbasi, P. Guerriero, M. Musiani, L. Vazquez-Gomez, E. Verlato, *ECS Electrochem. Lett.* **2013**, *2*, D58–D60; g) L. Mattarozzi, S. Cattarin, N. Comisso, A. Gambirasi, P. Guerriero, M. Musiani, L. Vázquez-Gómez, E. Verlato, *Electrochim. Acta* **2014**, *140*, 337–344; h) W. Siriwatcharapiboon, Y. Kwon, J. Yang, R. L. Chantry, Z. Li, S. L. Horswell, M. T. M. Koper, *ChemElectroChem* **2014**, *1*, 172–179; i) L. Mattarozzi, S. Cattarin, N. Comisso, R. Gerbasi, P. Guerriero, M. Musiani, L. Vázquez-Gómez, E. Verlato, *J. Electrochem. Soc.* **2015**, *162*, D236–D241; j) P. Mirzaei, S. Bastide, A. Aghajani, J. Bourgon, C. Zlotea, M. Laurent, M. Latroche, C. Cachet-Vivier, *Electrocatalysis* **2018**, *9*, 343–351; k) L. Mattarozzi, S. Cattarin, N. Comisso, N. El Habra, P. Guerriero, M. Musiani, L. Vázquez-Gómez, *Electrochim. Acta* **2020**, *346*, 136240; l) P. H. Van Langevelde, I. Katsounaros, M. T. M. Koper, *Joule* **2021**, *5*, 290–294; m) Z. X. Ge, T. J. Wang, Y. Ding, S. Bin Yin, F. M. Li, P. Chen, Y. Chen, *Adv. Energy Mater.* **2022**, *12*, 2103916.

[5] Z. Deng, C. Ma, Z. Li, Y. Luo, L. Zhang, S. Sun, Q. Liu, J. Du, Q. Lu, B. Zheng, X. Sun, *ACS Appl. Mater. Interfaces* **2022**, *14*, 46595–46602.

[6] a) G. Wang, P. Shen, Y. Luo, X. Li, X. Li, K. Chu, *Dalton Trans.* **2022**, *51*, 9206–9212; b) X. Xu, L. Hu, Z. Li, L. Xie, S. Sun, L. Zhang, J. Li, Y. Luo, X. Yan, M. S. Hamdy, Q. Kong, X. Sun, Q. Liu, *Sustain. Energy Fuels* **2022**, *6*, 4130–4136.

[7] Q. Liu, L. Xie, J. Liang, Y. Ren, Y. Wang, L. Zhang, L. Yue, T. Li, Y. Luo, N. Li, B. Tang, Y. Liu, S. Gao, A. A. Alshehri, I. Shakir, P. O. Agboola, Q. Kong, Q. Wang, D. Ma, X. Sun, *Small* **2022**, *18*, 2106961.

[8] Z. Li, J. Liang, Q. Liu, L. Xie, L. Zhang, Y. Ren, L. Yue, N. Li, B. Tang, A. A. Alshehri, M. S. Hamdy, Y. Luo, Q. Kong, X. Sun, *Mater. Today Phys.* **2022**, *23*, 100619.

[9] a) G. V. Gafanovich, L. S. Palatnik, *Met. Sci. Heat Treat.* **1974**, *16*, 808–810; b) D. Kutyła, A. Salcı, A. Kwiecińska, K. Kołczyk-Siedlecka, R. Kowalik, P. Żabiński, R. Solmaz, *Int. J. Hydrogen Energy* **2020**, *45*, 34805–34817.

[10] L. Huey-Lin, P. Duwez, *J. Less-Common Met.* **1964**, *6*, 248–249.

[11] P. Mirzaei, S. Bastide, A. Dassy, R. Bensimon, J. Bourgon, A. Aghajani, C. Zlotea, D. Muller-Bouvet, C. Cachet-Vivier, *Electrochim. Acta* **2019**, *297*, 715–724.

[12] Y. Liu, D. Gokcen, U. Bertocci, T. P. Moffat, *Science* **2012**, *338*, 1327–1330.

[13] a) K. Leistner, A. Krause, S. Fähler, H. Schlörb, L. Schultz, *Electrochim. Acta* **2006**, *52*, 170–176; b) R. Wang, U. Bertocci, H. Tan, L. A. Bendersky, T. P. Moffat, *J. Phys. Chem. C* **2016**, *120*, 16228–16237.

[14] F. A. Kröger, *J. Electrochem. Soc.* **1978**, *125*, 2028–2034.

[15] D. Pletcher, R. I. Urbina, *J. Electroanal. Chem.* **1997**, *421*, 145–151.

[16] A. Bard, L. Faulkner, *Electrochemical Methods: Fundamentals and Applications*, Wiley, New York, **2001**.

[17] B.-C. Yu, S.-K. Kim, J.-S. Sohn, B.-S. Kim, K.-I. Rhee, H.-J. Sohn, *J. Appl. Electrochem.* **2014**, *44*, 741–745.

[18] ICDD Card 00–005-0685, Rhodium.

[19] ICDD Card 00–004-0850, Nickel.

[20] ICDD Card 98–002-1505, Gold.